



Reduced interfacial recombination losses and lead leakage in lead-based perovskite solar cells using 2D/3D perovskite engineering

Huan Bi^{a,b}, Yao Guo^c, Mengna Guo^a, Chao Ding^b, Shuzi Hayase^b, Hanjun Zou^d, Qing Shen^{b,*}, Gaoyi Han^{a,**}, Wenjing Hou^{a,***}

^a Institute of Molecular Science, Key Laboratory of Materials for Energy Conversion and Storage of Shanxi Province, Shanxi University, Taiyuan, 030006, PR China

^b Faculty of Informatics and Engineering, The University of Electro-Communications, 1-5-1 Chofugaoka, Chofu, Tokyo, 182-8585, Japan

^c School of Materials Science and Engineering, Henan Joint International Research Laboratory of Nanocomposite Sensing Materials, Anyang Institute of Technology, Anyang, 455000, PR China

^d Analytical and Testing Center, Chongqing University, Chongqing, 401331, PR China



HIGHLIGHTS

- A new 2D modified material was employed in PSCs.
- The interfacial nonradiative recombination losses were reduced.
- The stability and efficiency are enhanced simultaneously after introducing MEMI.
- The energy level became more matchable with the HTL after MEMI modification.
- The lead leakage of water-soluble lead halide perovskite is suppressed.

ARTICLE INFO

Keywords:

Perovskite solar cell
2D/3D engineering
Defect passivation
Reducing lead leakage
Stability

ABSTRACT

Although perovskite solar cells (PSCs) have achieved significant success, there are still some barriers to their commercialization, such as poor stability and unsatisfactory power conversion efficiency (PCE). Here, we report low-dimensionality engineering of perovskites using mercaptoethylammonium iodide (MEMI). Two-dimensional (2D) perovskite materials can simultaneously passivate the interface defects of the perovskite film and enhance carrier extraction. The PCE of the device increased from 20.85% for the control device to a resultant of 22.41% for the target device. Meanwhile, device stability was ameliorated after MEMI modification, and the stability of unencapsulated target devices decreased by 7.5% after aging in the dark air condition for 300 h. Finally, the notorious lead leakage was significantly suppressed. This work guides to create efficient and stable environmentally friendly PSCs through low-dimensional engineering.

1. Introduction

The organic-inorganic perovskite solar cells (PSCs) have achieved a certified power conversion efficiency (PCE) of 25.7% [1] and are considered to be one of the most promising candidates for the next generation of photovoltaic technologies [2]. This is primarily related to the excellent features of the perovskite material, such as the low cost of raw material, high mobility, variable bandgap, strong extinction coefficient, and long carrier lifetime [3,4]. However, there are still some

concerns, such as lower PCE compared with the Shockley–Queisser theoretical limit efficiency, inferior long-term stability, terrible lead leak, and other potential problems. Therefore, solving these problems is extremely important.

It is well known that reducing interfacial non-radiative recombination is essential for improving the performance of PSCs. To date, various strategies have been developed to reduce non-radiative recombination at the interface, such as inorganic interface modification [5], organic interface modifications [4,6], Two-dimensional (2D) perovskite

* Corresponding author.

** Corresponding author.

*** Corresponding author.

E-mail addresses: shen@pc.uec.ac.jp (Q. Shen), han_gaoyis@sxu.edu.cn (G. Han), houwenjing@sxu.edu.cn (W. Hou).

(2D-PVK) engineering [7–9], and polymer modification [10,11]. Among them, modified engineering has proven to be an effective strategy because it can passivate interface defects, adjust the energy level, and enhance the moisture stability of PSCs simultaneously [12,13]. To date, a series of organic spacer cations have been developed for interface dimensionality engineering. Li et al. synthesized a new 2D material, 2-(2-pyridyl)ethylamine iodide (2-PyEAI), to modify the top contact interface [7]. 2D/3D (3D: three-dimensional) PSCs based on 2-PyEAI modification show high-quality perovskite films, few defect states, matched energy levels, and a long carrier lifetime. Consequently, the dual-optimized PSC has obtained a champion PCE of 23.2%, accompanied by superior stability. Liu et al. developed a series of organic spacer cations, such as benzimidine hydrochloride (PhFACl), 4-hydroxybenzimidinium hydrochloride (*p*-HOPhFACl), and 4-fluorobenzimidinium hydrochloride (*p*-FPhFACl) to improve the PCE and stability of PSCs [8]. However, compared with the diversity of organic molecules, the number and variety of organic spacer cations are insufficient. Therefore, the development of new and effective 2D modification materials is urgently required.

In addition, lead leakage is an inevitable problem in lead-based PSCs. A large amount of lead leakage can exert an irreversible and devastating impact on human and animal physical functions [14,15]. Thus, various studies have been conducted to avoid or reduce lead leakage through gas post-treatment [16], device packaging [15], interface engineering [17], etc. [18] Among these, interface engineering has attracted extensive

attention owing to its simplicity. However, interface engineering has received relatively little scientific attention. Therefore, it is developing a simpler and effective interface strategy for preventing lead leakage is urgent.

In this study, a new 2D material, mercaptoethylammonium iodide (MEMI), was synthesized and used to enhance the PCE and stability of PSCs and to prevent lead leakage. After MEMI modification, the device exhibited reduced interface defects, improved carrier extraction, and enhanced PCE and stability. The device modified by MEMI achieved a PCE of 22.41%. After aging in the dark air condition (25 °C, 10–15 RH%) for 300 h, the unencapsulated modified device maintained 92.5% of its initial PCE. In addition, lead leakage was significantly inhibited after MEMI was modified. This work highlights the critical role of low-dimensional perovskite interface engineering in realizing highly efficient and stable methylammonium-free (MA-free) PSCs.

2. Results and discussion

As shown in Fig. 1a, the device structure used in this work ought to be FTO/TiO₂/Rb_{0.02}(FA_{0.95}Cs_{0.05})_{0.98}PbI_{2.91}Br_{0.03}Cl_{0.06} (3D)/2D-PVK/Spiro-OMeTAD/Ag, in which the MEMI was modified on the surface of the 3D perovskite to form the 2D Ruddlesden–Popper (RP) perovskite by van der Waals forces. X-ray photoelectron spectroscopy (XPS) was employed to determine the possible chemical interactions between MEMI and the perovskite (Fig. 1b). After MEMI modification, XPS peaks

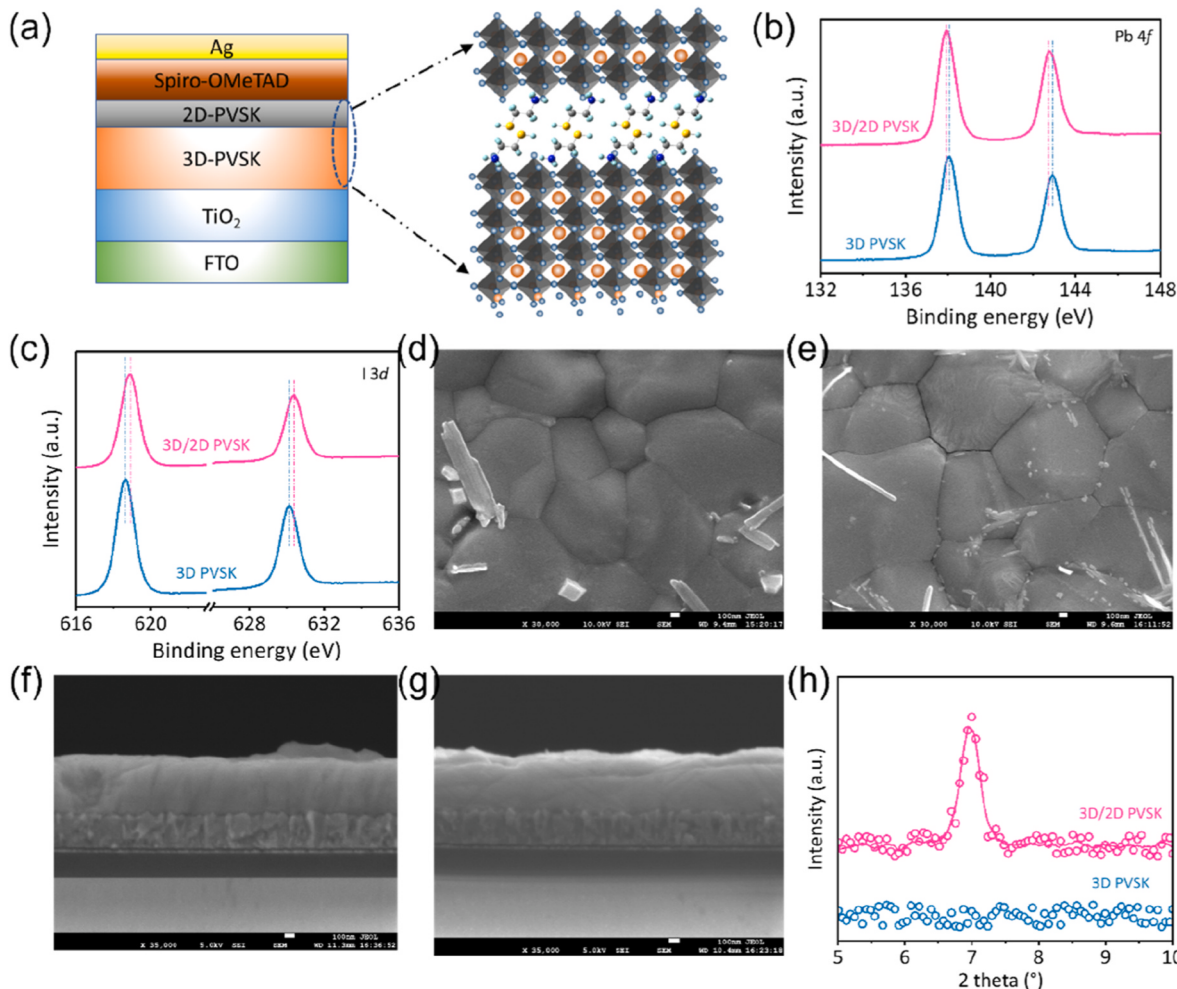


Fig. 1. (a) Structure of MEMI-modified device; XPS spectra of (b) Pb 4f and (c) I 3d perovskite film without and with MEMI modification. Top-view SEM images of (d) pure perovskite and (e) MEMI-modified perovskite films. Cross-sectional SEM images of (f) control and (g) target perovskite films deposited on FTO/TiO₂. (h) XRD patterns of the control sample and target sample.

of Pb 4f_{7/2} and Pb 4f_{5/2} peaks shifted from 138.05 to 142.90 eV of the control film to 137.95 and 142.75 eV, respectively [5,19,20]. Generally, a lower-shifted XPS peak suggests an increased electron cloud density around Pb²⁺ ions. In addition, the XPS peaks of I 3d of the target perovskite film shifted to a higher binding energy than that of the control film (Fig. 1c). The significantly shifted XPS peaks (Pb 4f and I 3d) suggested a strong chemical interaction between the 3D perovskite and MEMI, which was primarily owing to the formation of RP-2D perovskite [3,5,20,21]. The top view of the scanning electron microscope (SEM) was employed to investigate the effect of MEMI modification on the morphology of the perovskite film. As displayed in Fig. 1d and e, there were no obvious changes in the grain size after modification with MEMI, which indicated that MEMI did not significantly affect the morphology of the perovskite films. The rear section of the thin film can be seen in the cross-view SEM images (Fig. 1f and g). The thickness of the perovskite film was not significantly different and could reach approximately 585 nm, which is a competitive thickness and would result in a high short-circuit current density (J_{SC}) in PSCs. X-ray diffraction (XRD) patterns were obtained to study the generation of the 2D perovskites. As illustrated in Fig. 1h, a prominent diffraction peak appeared at 7° after MEMI modification [22–24], which supports the generation of 2D perovskite. As shown in ultraviolet-visible (UV-vis) absorption spectra in Fig. S1, the intensity of the UV-vis absorption curve was slightly enhanced in the range of 550–750 nm after the MEMI modification.

Subsequently, we studied the effect of interface modification on the quality of perovskite films. First, steady-state photoluminescence (PL)

and time-resolved photoluminescence (TRPL) techniques were employed as effective methods to uncover the effect of MEMI on defects in perovskite films. As illustrated in Fig. 2a, the PL peak intensity of the target film (glass/3D-perovskite/MEMI) was higher than that of the pure perovskite film (glass/3D-perovskite), implying that the defects can be passivated by forming a 2D perovskite. In addition, as shown in Fig. 2b, some peaks can be seen at a lower wavelength for the target perovskite film, which also suggests that a 2D perovskite was generated. According to our previous work, the TRPL dynamics were fitted well using the double-exponential function [3,5]:

$$I(t) = A_1 e^{\left(\frac{-t}{\tau_1}\right)} + A_2 e^{\left(\frac{-t}{\tau_2}\right)} \quad (1)$$

$$\tau_{ave} = \frac{A_1 \tau_1^2 + A_2 \tau_2^2}{A_1 \tau_1 + A_2 \tau_2} \quad (2)$$

where τ_1 and τ_2 are the fast and slow decay lifetime constants, respectively, and A_1 and A_2 are the amplitudes of the fast and slow decay processes, respectively. The average carrier lifetime (τ_{ave}) was calculated using Equation (2), and the fitting results are displayed in Table S1. The average carrier lifetime of the target perovskite film was 72.78 ns, which is higher than that of the control film (54.15 ns). Longer carrier lifetimes result in fewer film defects. The PL intensity mapping images indicated the same trend as the PL curves (Fig. 2d–e). Meanwhile, the PL peak position of the target film was blue-shifted (Fig. 2f–g). Universally, a lower wavelength indicates fewer defects in the perovskite film.

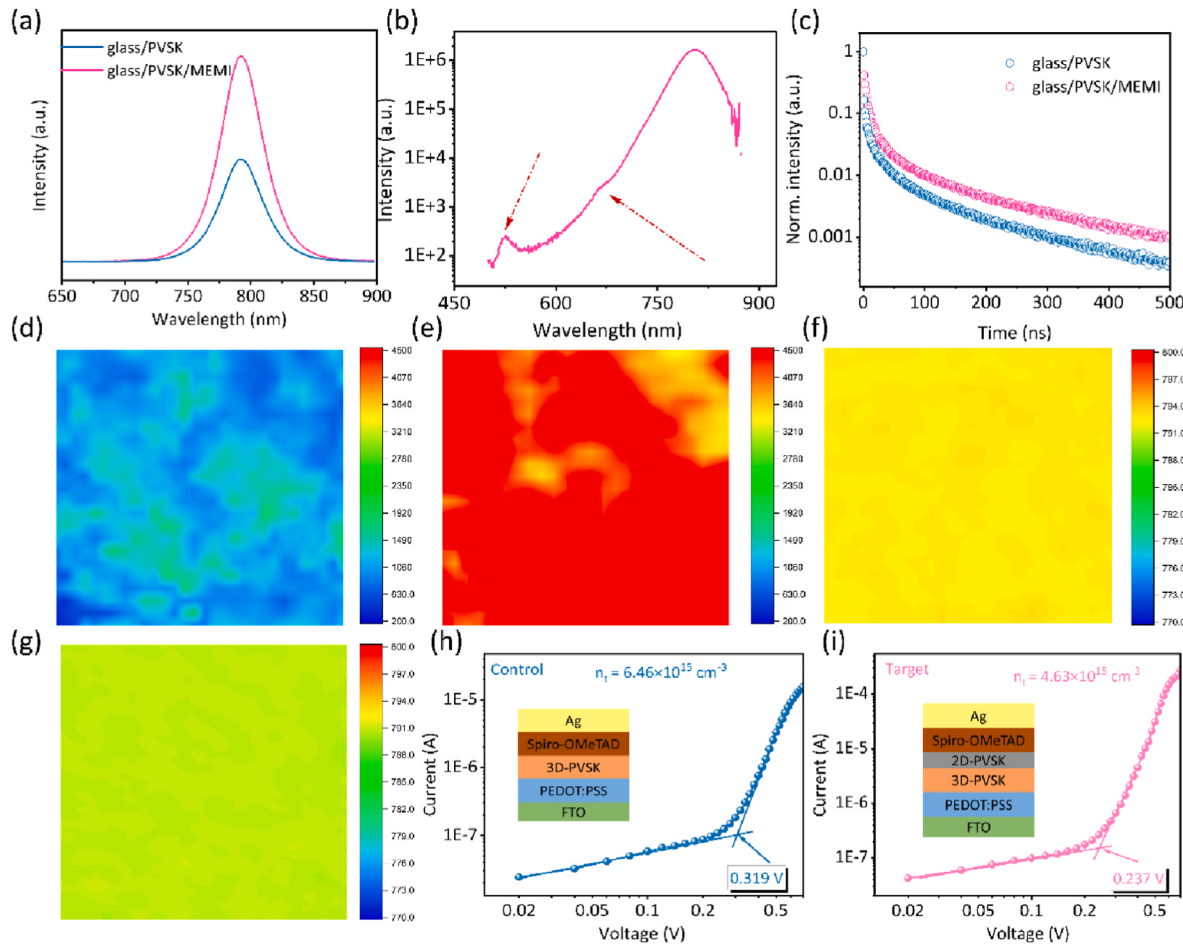


Fig. 2. (a) PL spectra of the perovskite films with glass/perovskite and glass/perovskite/MEMI structures. (b) PL spectra of target film with log treated. (c) TRPL curves of perovskite with and without MEMI modification. PL intensity mapping images of (d) control and (e) target perovskite films. PL peak position mapping images of (f) control and (g) target perovskite films. Dark I–V curves of the device FTO/PEDOT:PSS/perovskite/spiro-OMeTAD/Ag based on (h) pristine and (i) MEMI-modified perovskite films.

Space-charge limited currents (SCLC) were used to estimate the defects in the perovskite film with or without MEMI modification using hole-only devices (FTO/PEDOT:PSS/perovskite/(MEMI)/Spiro-OMeTAD/Ag). In the dark *I-V* curve, the voltage at the kink point between the ohmic and trap filling regions is defined as the trap filling limit voltage (V_{TFL}). The defect density was calculated using the equation $n_t = (2\epsilon\epsilon_0 V_{TFL})/(eL^2)$ [19,25], where ϵ_0 is the permittivity of free space., ϵ is the vacuum permittivity of the perovskite, e is the elementary charge, and L is the thickness of the perovskite film. As shown in Fig. 2h and i, the defect density was reduced from $6.46 \times 10^{15} \text{ cm}^{-3}$ for the control perovskite film to $4.63 \times 10^{15} \text{ cm}^{-3}$ for the MEMI-modified perovskite film. In summary, the defects of the film were reduced after the formation of the RP-2D perovskite.

To gain a deeper insight into the carrier transfer and recombination for the devices with and without MEMI modification, devices with glass/perovskite/spiro-OMeTAD and glass/perovskite/MEMI/spiro-OMeTAD structures were employed to test the PL and TRPL. As shown in Fig. 3a, the PL intensity decreased when the 2D/3D heterojunction was formed, indicating that carrier extraction was improved. Furthermore, reduced carrier lifetimes (Fig. 3b and Table S2, Control: $\tau_1 = 4.44 \text{ ns}$, $\tau_2 = 20.71 \text{ ns}$, $\tau_{ave} = 15.88 \text{ ns}$; Target: $\tau_1 = 4.13 \text{ ns}$, $\tau_2 = 17.57 \text{ ns}$, $\tau_{ave} = 11.38 \text{ ns}$) also confirmed that carrier extraction was improved after MEMI modification. As shown in Fig. 3c and d, the Spiro-OMeTAD coated perovskite film on the glass substrate was used to test the PL mapping, which demonstrated the same trend as the PL curve (Fig. 3a). Electrochemical impedance spectroscopy (EIS) was performed to determine the effect of MEMI on the carrier transfer and recombination. Fig. 3e exhibits the Nyquist plots of the PSCs with and without MEMI modification, which was measured at a bias of 0 V in the frequency range of 1 MHz to 0.1 Hz under dark conditions. It has been confirmed from the literature that the semicircle in the high-frequency region is related to charge-transfer resistance (R_{ct}) and the low-frequency region is ascribed to recombination resistance (R_{rec}) [5,26]. R_{ct} was decreased and R_{rec} was increased after MEMI was modified, which confirmed the promotion of interfacial charge transfer and suppression of charge recombination. The increase in R_{rec} can be attributed to the decreased number of defects in the film. In addition, an increase in carrier lifetime can be attributed to increased R_{rec} . *C-V* measurements can provide

information about the semiconductor interface and charge transport. Fig. S2 displays the Mott–Schottky plots of the devices with and without MEMI modification. The built-in potentials (V_{bi}) of the control and target devices were 0.76 and 0.87 V, respectively. Moreover, an increased V_{bi} after MEMI modification promoted carrier transport. These results are consistent with those of TRPL and EIS. Ultraviolet photo-electron spectroscopy (UPS) was utilized to estimate the influence of MEMI on the surface energy levels of the perovskite (Fig. 3f and Figs. S3–4). The conduction band minimum (CBM) and valence band maximum (VBM) were calculated according to previous studies [4]. After the MEMI modification, the energy levels of the 2D/3D perovskite film were better matched with those of Spiro-OMeTAD. Furthermore, a suitable energy level can also reduce the charge accumulation at the interface.

Significantly reduced film defects and improved carrier dynamics stimulated us to explore the impact of MEMI on the photovoltaic performance of the PSCs, and the results are exhibited in Fig. 4a, Figs. S5–7, and Table S3. All photovoltaic parameters (J_{SC} , open-circuit voltage V_{OC} , fill factor (FF), and PCE) first increased and then decreased with the increase in MEMI concentration, and reached their maximum values when the concentration of MEMI was 1 mg/mL. The average PCE of the control device was $20.72\% \pm 0.135$ while that of the target device was $22.19\% \pm 0.218$. The average V_{OC} and FF increased from $1.072 \text{ V} \pm 0.004 \text{ V}$ and $0.777 \text{ V} \pm 0.011 \text{ V}$ for the control device to $1.102 \text{ V} \pm 0.007 \text{ V}$ and $0.793 \text{ V} \pm 0.015 \text{ V}$ for the target device, respectively. The improvement in V_{OC} and FF was primarily due to the reduction in non-radiative recombination and defects. Fig. 4b shows the typical *J-V* curves of the control and target devices in the forward-scanned (FS) and reverse-scanned (RS) directions. The control device delivered an FS PCE of 20.85% (J_{SC} of 24.76 mA/cm^2 , V_{OC} of 1.074 V , and FF of 0.785), whereas the MEMI-modified device exhibited an enhanced FS PCE of 22.41% (J_{SC} of 25.27 mA/cm^2 , V_{OC} of 1.106 V , and FF of 0.802). The incident photon-to-current efficiency (IPCE) of the device is shown in Fig. 4c. The integrated J_{SC} value for the control device and MEMI-treated device was up to 24.23 mA/cm^2 and 24.90 mA/cm^2 , respectively, which was consistent with the J_{SC} value obtained from the *J-V* curves. The steady-state output current density and PCE for the control and target PSCs at the maximum power point under one-sun illumination for 500 s

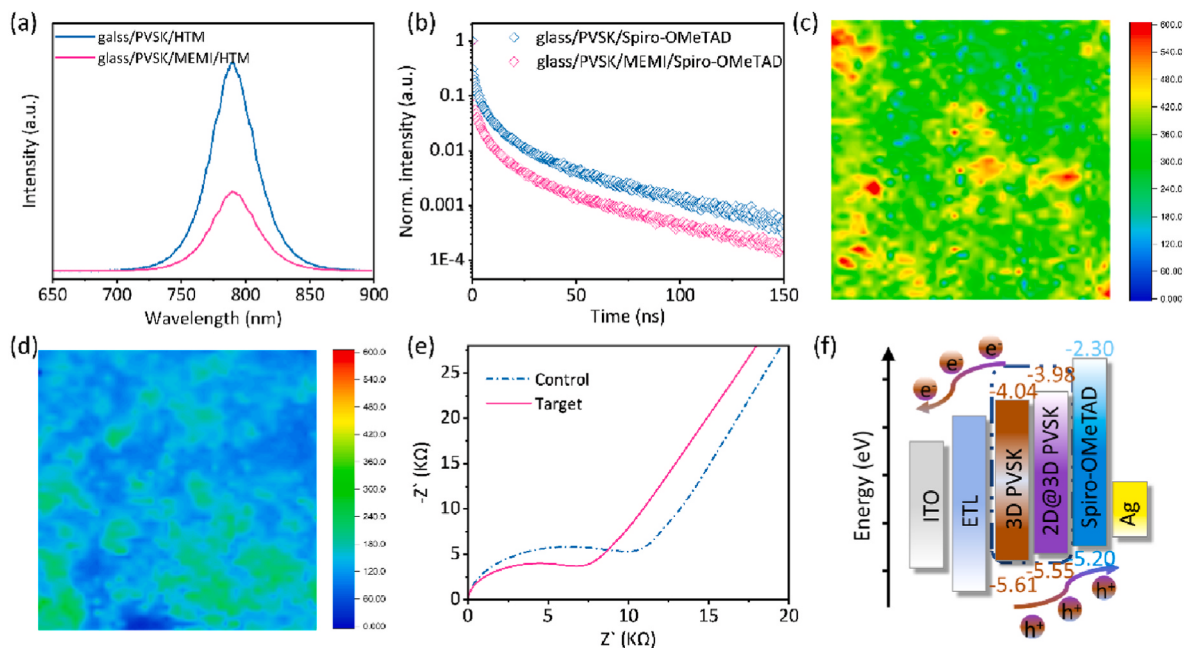


Fig. 3. (a) PL and (b) TRPL spectra of the control and target perovskite films with glass/perovskite/spiro-OMeTAD and glass/perovskite/MEMI/spiro-OMeTAD structures. PL mapping of (c) control and (d) target film. (e) Nyquist plots of the control device and target device measured at the frequency ranging from 1 MHz to 0.1 Hz with a bias of 0 V. (f) Energy level diagram of the device components in present work.

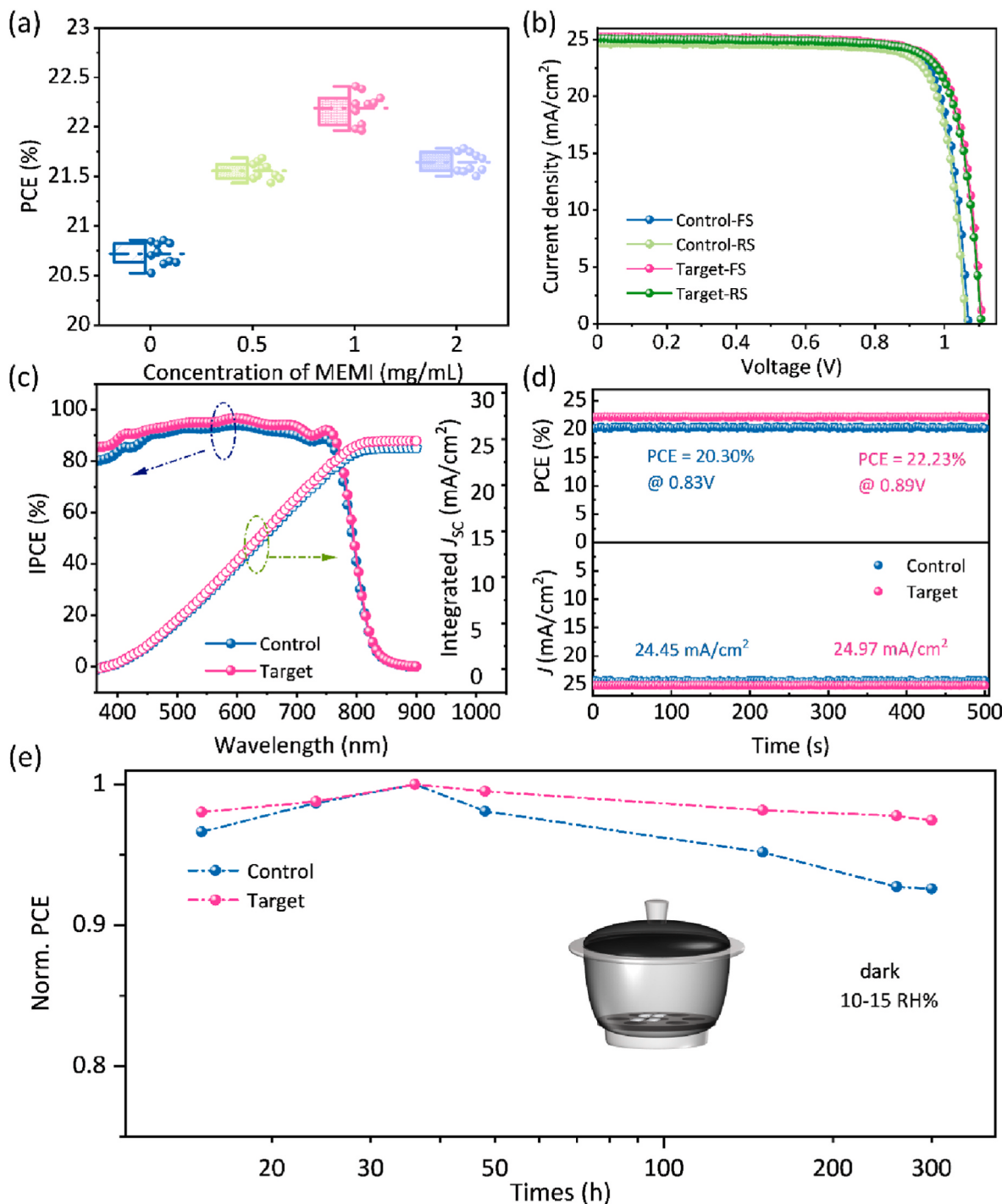


Fig. 4. (a) Statistical PCE of the PSCs modified by different concentrations of MEMI. (b) J - V curves of the best-performing control device and the MEMI-modified devices. J - V curves were measured in reverse scan (RS) and forward scan (FS) at a scan rate of 120 mV/s under simulated AM 1.5G one sun illumination of 100 mW/cm² (c) IPCE spectra along with corresponding integrated current density curves of the best-performing control and target devices. (d) Stabilized PCE and the photocurrent density at maximum power point of the best-performing devices with and without MEMI. (e) Ambient stability of the unencapsulated control and target devices with 10–15 RH% at room temperature in the dark condition.

are shown in Fig. 4d. The stabilized current density and PCE increased from 24.45 mA/cm² and 20.30% for the control device ($V_{p\text{-max}} = 0.83$ V) to 24.97 mA/cm² and 22.23% for 2D/3D device ($V_{p\text{-max}} = 0.89$ V). The stable PCE response curve of the MEMI-modified devices implies that they have better light stability. In addition to the PCE, the stability of the devices is another key factor in commercial applications. Therefore, a stability test was employed to evaluate the stability of the unencapsulated devices with and without 2D engineering. The long-term stability

test was implemented in ambient conditions with a relative humidity range of 10–15 RH% at room temperature (28–35 °C). The photovoltaic parameters are shown in Fig. 4e and Fig. S8. After aging for 300 h, the control device maintained 92.5% of its initial PCE, whereas the target device maintained 98% of its initial PCE. The improved stability of the target device can be attributed to these factors.

- 1) Fewer defects at the interface after the MEMI treatment can reduce the corrosion sites of water.
- 2) There is a strong chemical interaction between MEMI and perovskite such as MEMI-Pb.
- 3) The formed 2D perovskite has excellent water stability.

Pb-based PSCs have been criticized for their notorious lead leakage. Therefore, it is necessary to evaluate the lead leakage of devices after MEMI modification. We evaluated the lead leakage by immersing the devices in water. As shown in Fig. 5a, after 30 s, the target film remained black, whereas the control film became yellow. After 15 min, a large amount of the perovskite film dissolved in water for the control film, whereas the target film did not dissolve much. The lower the dissolution of the film in water, the more environmentally friendly is the device. Inductively coupled plasma mass spectrometry (ICP-MS) measurements were used to estimate the concentration of Pb that leaked from the perovskite to the water. As displayed in Fig. 5b, an obvious regular pattern can be seen in which the concentration of Pb decreased with an increase in the concentration of MEMI. The lead content for the control device was up to 5 mg/L, while the target device only showed a lead content of 0.9 mg/L. The ultralow lead leakage was not only attributed to the strong chemical interaction between MEMI and Pb^{2+} in the perovskite film, but also to the formation of a hydrophobic 2D perovskite layer. Therefore, 2D engineering can not only improve the PCE and stability of the device but also reduce the leakage of lead.

3. Conclusion

In summary, we have demonstrated a 2D interface modification layer to enhance the performance of MA-free PSCs. XPS measurements proved that there is indeed a strong chemical link between MEMI and perovskite. The 2D/3D heterojunction engineering strategy led to defect passivation and improved the hole extraction. The PCE of the 2D/3D heterojunction device increased from 20.85% to 22.41% because of the significantly suppressed non-radiative recombination losses. The stability of the PSCs was also improved as a result of the 2D layer formed by MEMI. Finally, we evaluated the lead leak rate of PSCs with or without MEMI treatment and found that less lead leakage occurred after MEMI modification. This study provides a positive strategy for fabricating highly efficient, stable, and environmentally friendly PSCs. Moreover, it also guides the commercialization of PSCs.

4. Experimental section

4.1. Materials and solvents

Lead (II) bromide (PbBr_2 , 99.9%), formamidine hydroiodide (FAI, 99.9%), bis(trifluoromethane) sulfonimide lithium salt (Li-TFSI, 99%), 2,2',7,7'-tetrakis [*N,N*-di (4-methoxyphenyl)amino]-9,9'-spirobifluorene (Spiro-OMeTAD, 99.86%), and 4-*tert*-butyl pyridine (tBP, 99%)

were purchased from Advanced Election Technology Co. Ltd. Lead (II) iodide (PbI_2 , 99.99%), mercaptoethylammonium iodide (MEMI), lead (II) chloride (PbCl_2 , 99.99%) and methylamine hydrochloride (MACl, 99.5%) were purchased from Xi'an Polymer Light Technology Corp. Cesium iodide (CsI, 99.99%) and rubidium iodide (RbI) were obtained from Aladdin. Acetonitrile (ACN, 99.8%) was obtained from Macklin. Titanium tetrachloride (TiCl_4), chlorobenzene (CB >99.9% purity), N, N-dimethylformamide (DMF, 99.8%), and dimethyl sulfoxide (DMSO, 99.8%) were purchased from Sigma-Aldrich. All chemicals were used without further purification.

4.2. Device fabrication

Laser-patterned fluorine-doped tin oxide (FTO) glasses (purchased from Jiangsu Yanchang Sunlaite New Energy Co., Ltd.) were ultrasonically cleaned with detergent water and ethanol for 20 min in sequence. After being dried by nitrogen (99.99%), the FTO was treated with ultraviolet ozone (UV-O_3) for 30 min. For the preparation of TiO_2 electron transport layer, the FTO glass substrate was put into aqueous solution of TiCl_4 ($\text{TiCl}_4:\text{H}_2\text{O} = 2.25:1$, V:V) for 45 min at 70 °C. The substrates were then washed and annealed at 200 °C for 30 min. When the substrates cooled to room temperature, they were treated with UV-O_3 for 20 min. All the substrates were then transferred to an argon-filled glovebox for perovskite deposition. A 1.55 M perovskite ($\text{Rb}_{0.02}(\text{FA}_{0.95}\text{Cs}_{0.05})_{0.98}\text{PbI}_{2.91}\text{Br}_{0.03}\text{Cl}_{0.06}$) precursor solution was prepared by dissolving 248.16 mg FAI, 19.73 mg CsI, 6.58 mg RbI, 682.73 mg PbI_2 , 8.53 mg PbBr_2 , 12.74 mg PbCl_2 , and 35 mg MACl (additive) in the mixed solvents of DMF and DMSO ($V_{\text{DMF}}:V_{\text{DMSO}} = 4:1$). The as-prepared perovskite precursor solution was filtered using a 0.22 μm PTFE filter before use. The perovskite film was deposited by spin-coating the precursor solution at 4000 rpm for 30 s 80 μL CB antisolvent was dripped on perovskite films at 16 s before ending the program, and the film was then annealed at 130 °C for 30 min. For MEMI treatment, different concentrations of MEMI (0, 0.5, 1, and 2 mg/mL) were dissolved in isopropyl alcohol, and then 40 μL of MEMI was spin-coated on the perovskite film at a speed of 5000 rpm for the 30 s, then annealed at 100 °C for 10 min. The spiro-OMeTAD solution was prepared by mixing 72.3 mg spiro-OMeTAD, 28.8 μL 4-*tert*-butyl pyridine (tBP) and 17.5 μL lithium bis(trifluoromethane sulfonyl)imide (Li-TFSI) stock solution (520 mg Li-TFSI in 1 mL acetonitrile) in 1 mL CB. Subsequently, 20 μL of Spiro-OMeTAD solution was spin-coated onto the perovskite films at 4000 rpm for 33 s to form the hole transport layer. Finally, approximately 100 nm metal counter electrode was thermally evaporated on top of the spiro-OMeTAD film under a vacuum of 3×10^{-4} Pa using a shadow mask.

4.3. Characterization

J-V curves were obtained using a solar simulator equipped with a Keithley 2400 source meter, and a black metal mask was employed to define the effective active area of the device to be 0.1 cm². The *J-V*

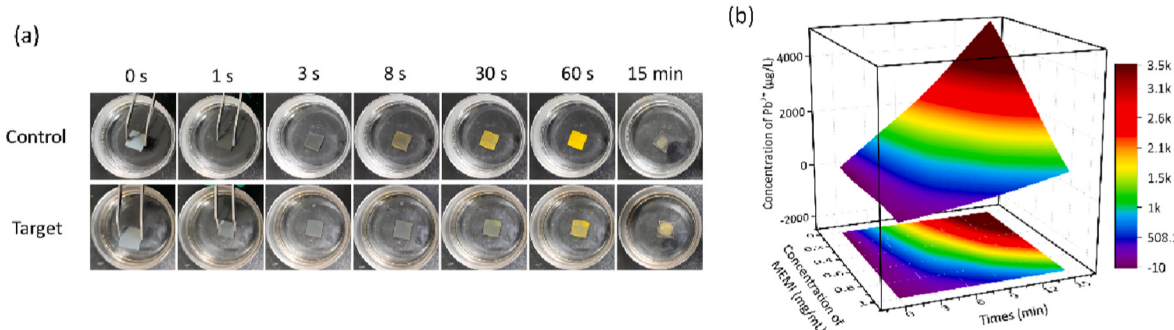


Fig. 5. (a) Pictures of the film with and without MEMI modification were soaked in water at different times. (b) Pb concentration was measured by ICP-MS. Photo credit: Huan Bi, The University of Electro-Communication.

curves were measured at a scan rate of 120 mV/s. The PCE of the PSCs was tested under normal air conditions. UV–Vis spectra were measured on an Agilent 8453 UV–Vis G1103A spectrometer. Photoluminescence (PL) spectra was recorded using a Confocal Raman system (iHR 550 HORIBA) with a laser of 532 nm. XPS spectra were collected using a Physical Electronics Model 5700 XPS instrument, and the data were analyzed and processed using Thermo Avantage (v5.9921) software. SEM observations were performed on SEM (FESEM, JEOL-JSM-6701 F) in ADD mode. The structural properties were characterized using an X-ray diffractometer (XRD) (D2 PHASER Desktop XRD, BRUKER, Germany). Ultraviolet photoelectron spectroscopy (UPS) was performed using a PHI 5000 VersaProbe III with a He I source (21.22 eV) under an applied negative bias of 9.0 V. Energy-dispersive X-ray spectroscopy (EDS) measurements were carried out using a field-emission scanning electron microscope (JEM-7900 F, Japan) with EDS equipment. Pb concentration in the water was detected using an ICP–MS instrument (NexION 350, PerkinElmer). Time-resolved photoluminescence (TRPL) was measured using a self-built scanning confocal system based on an inverted microscope (Nikon, TE2000-U) with a 450 nm laser at the State Key Laboratory of Quantum Optics and Quantum Optics Devices of Shanxi University.

CRediT authorship contribution statement

Huan Bi: Conceptualization, Validation, Investigation, Writing – original draft, Writing – review & editing. **Yao Guo:** Validation. **Mengna Guo:** Validation. **Chao Ding:** Resources. **Shuzi Hayase:** Resources, Funding acquisition. **Hanjun Zou:** Resources. **Qing Shen:** Conceptualization, Resources, Writing – review & editing, Supervision. **Gaoyi Han:** Validation, Resources, Supervision, Funding acquisition. **Wenjing Hou:** Validation, Resources, Writing – review & editing, Supervision, Funding acquisition.

Declaration of competing interest

The authors declare that they have no known competing financial interests or personal relationships that could have appeared to influence the work reported in this paper.

Data availability

Data will be made available on request.

Acknowledgements

This work was financially supported by the National Natural Science Foundation of China (61804091, and U21A6004), Scientific and Technological Innovation Programs of Higher Education Institutions in Shanxi (2020L0002), Natural Science Foundation of Shanxi Province under Grant (201901D211127), and Program of State Key Laboratory of Quantum Optics and Quantum Optics Devices (No: KF201910). We are grateful to the Scientific Research Start-up Funds of Shanxi University and the Hundred Talents Plan of the Shanxi Province. This research was partly supported by the Japan Science and Technology Agency (JST) Mirai program (JPMJMI17EA). We would also like to thank Shiyanjia Lab (www.shiyanjia.com) in supporting to conduct the tests.

Appendix A. Supplementary data

Supplementary data to this article can be found online at <https://doi.org/10.1016/j.jpowsour.2023.232825>.

References

- [1] NREL. <https://www.nrel.gov/pv/cell-efficiency.html>.
- [2] Z.W. Gao, Y. Wang, W.C.H. Choy, Buried interface modification in perovskite solar cells: a materials perspective, *Adv. Energy Mater.* 12 (2022), 2104030, <https://doi.org/10.1002/aenm.202104030>.
- [3] H. Bi, X. Zuo, B. Liu, D. He, L. Bai, et al., Multifunctional organic ammonium salt-modified SnO₂ nanoparticles toward efficient and stable planar perovskite solar cells, *J. Mater. Chem. 9* (2021) 3940–3951, <https://doi.org/10.1039/DOTA12612H>.
- [4] X. Zuo, B. Kim, B. Liu, D. He, L. Bai, et al., Passivating buried interface via self-assembled novel sulfonium salt toward stable and efficient perovskite solar cells, *Chem. Eng. J.* 1 (2021), 133209, <https://doi.org/10.1016/j.cej.2021.133209>.
- [5] H. Bi, B. Liu, D. He, L. Bai, W. Wang, et al., Interfacial defect passivation and stress release by multifunctional KPF₆ modification for planar perovskite solar cells with enhanced efficiency and stability, *Chem. Eng. J.* 418 (2021), 129375, <https://doi.org/10.1016/j.cej.2021.129375>.
- [6] F. Zhang, S. Ye, H. Zhang, F. Zhou, Y. Hao, et al., Comprehensive passivation strategy for achieving inverted perovskite solar cells with efficiency exceeding 23% by trap passivation and ion constraint, *Nano Energy* 89 (2021), 106370, <https://doi.org/10.1016/j.nanoen.2021.106370>.
- [7] G. Li, J. Song, J. Wu, Z. Song, X. Wang, et al., Efficient and stable 2d@3d/2D perovskite solar cells based on dual optimization of grain boundary and interface, *ACS Energy Lett.* 6 (2021) 3614–3623, <https://doi.org/10.1021/acsenergylett.1c01649>.
- [8] T. Liu, J. Guo, D. Lu, Z. Xu, Q. Fu, et al., Spacer engineering using aromatic formamidinium in 2D/3D hybrid perovskites for highly efficient solar cells, *ACS Nano* 15 (2021) 7811–7820, <https://doi.org/10.1021/acsnano.1c02191>.
- [9] S. Shao, M. Nijenhuis, J. Dong, S. Kahmann, G. ten Brink, et al., Influence of the stoichiometry of tin-based 2D/3D perovskite active layer on solar cells performances, *J. Mater. Chem. 9* (2021) 10095–10103, <https://doi.org/10.1039/dota10277f>.
- [10] H. Zhang, X. Ren, X. Chen, J. Mao, J. Cheng, et al., Improving the stability and performance of perovskite solar cells via off-the-shelf post-device ligand treatment, *Energy Environ. Sci.* 11 (2018) 2253–2262, <https://doi.org/10.1039/c8ee00580j>.
- [11] J. Wei, F. Guo, X. Wang, K. Xu, M. Lei, et al., SnO₂-in-Polymer matrix for high-efficiency perovskite solar cells with improved reproducibility and stability, *Adv. Mater.* 30 (2018), 1805153, <https://doi.org/10.1002/adma.201805153>.
- [12] A.A. Sutanto, P. Caprioglio, N. Drigo, Y.J. Hofstetter, I. Garcia-Benito, et al., 2D/3D perovskite engineering eliminates interfacial recombination losses in hybrid perovskite solar cells, *Chem* 7 (2021) 1903–1916, <https://doi.org/10.1016/j.chempr.2021.04.002>.
- [13] C. Deng, J. Wu, Y. Du, Q. Chen, Z. Song, et al., Surface reconstruction and in situ formation of 2D layer for efficient and stable 2D/3D perovskite solar cells, *Small Methods* 5 (2021), 2101000, <https://doi.org/10.1002/smtm.202101000>.
- [14] X. Wei, M. Xiao, B. Wang, C. Wang, Y. Li, et al., Avoiding structural collapse to reduce lead leakage in perovskite photovoltaics, *Angew. Chem. Int. Ed. Engl.* (2022), e202204314, <https://doi.org/10.1002/anie.202204314>.
- [15] X. Li, F. Zhang, J. Wang, J. Tong, T. Xu, et al., On-device lead-absorbing Tapes for sustainable perovskite solar cells, *Nat. Sustain.* 4 (2021) 1038–1041, <https://doi.org/10.1038/s41893-021-00789-1>.
- [16] H. Zhang, K. Li, M. Sun, F. Wang, H. Wang, et al., Design of superhydrophobic surfaces for stable perovskite solar cells with reducing lead leakage, *Adv. Energy Mater.* 11 (2021), 2102281, <https://doi.org/10.1002/aenm.202102281>.
- [17] S. Wu, Z. Li, M.-Q. Li, Y. Diao, F. Lin, et al., 2D metal–organic framework for stable perovskite solar cells with minimized lead leakage, *Nat. Nanotechnol.* 15 (2020) 934–940, <https://doi.org/10.1038/s41565-020-0765-7>.
- [18] Y. Hu, W. Song, X. Wang, X. Shi, X. Jia, et al., A holistic sunscreen interface strategy to effectively improve the performance of perovskite solar cells and prevent lead leakage, *Chem. Eng. J.* 433 (2022), 134566, <https://doi.org/10.1016/j.cej.2022.134566>.
- [19] W. Gao, H. Dong, N. Sun, L. Chao, W. Hui, et al., Chiral cation promoted interfacial charge extraction for efficient tin-based perovskite solar cells, *J. Energy Chem.* 68 (2022) 789–796, <https://doi.org/10.1016/j.jechem.2021.09.019>.
- [20] X. Zuo, B. Kim, B. Liu, D. He, L. Bai, et al., Passivating buried interface via self-assembled novel sulfonium salt toward stable and efficient perovskite solar cells, *Chem. Eng. J.* 431 (2021), 133209, <https://doi.org/10.1016/j.cej.2021.133209>.
- [21] B. Liu, H. Bi, D. He, L. Bai, W. Wang, et al., Interfacial defect passivation and stress release via multi-active-site ligand anchoring enables efficient and stable methylammonium-free perovskite solar cells, *ACS Energy Lett.* 6 (2021) 2526–2538, <https://doi.org/10.1021/acsenergylett.1c00794>.
- [22] B. Liu, J. Hu, D. He, L. Bai, Q. Zhou, et al., Simultaneous passivation of bulk and interface defects with gradient 2D/3D heterojunction engineering for efficient and stable perovskite solar cells, *ACS Appl. Mater. 14* (2022) 21079–21088, <https://doi.org/10.1021/acsami.2c04374>.
- [23] S. Gharibzadeh, B. Abdollahi Nejand, M. Jakoby, T. Abzieher, D. Hauschild, et al., Record open-circuit voltage wide-bandgap perovskite solar cells utilizing 2D/3D perovskite heterostructure, *Adv. Energy Mater.* 9 (2019), 1803699, <https://doi.org/10.1002/aenm.201803699>.
- [24] Q. Zhou, L. Liang, J. Hu, B. Cao, L. Yang, et al., High-performance perovskite solar cells with enhanced environmental stability based on a (p-FC₆H₄C₂H₄NH₃)₂[PbI₄] capping layer, *Adv. Energy Mater.* 9 (2019), 1802595, <https://doi.org/10.1002/aenm.201802595>.
- [25] C. Luo, G. Zheng, F. Gao, X. Wang, Y. Zhao, et al., Facet orientation tailoring via 2D-seed-induced growth enables highly efficient and stable perovskite solar cells, *Joule* 6 (2022) 240–257, <https://doi.org/10.1016/j.joule.2021.12.006>.
- [26] R. Zhao, L. Xie, R. Zhuang, T. Wu, R. Zhao, et al., Interfacial defect passivation and charge carrier management for efficient perovskite solar cells via a highly

crystalline polymer, ACS Energy Lett. 6 (2021) 4209–4219, <https://doi.org/10.1021/acsenergylett.1c01898>.